Tracking brain maturation *in vivo*: functional connectivity, white matter integrity, and synaptic density in developing mice

Charissa Millevert,[a,b,f] Nicholas Vidas-Guscic,[c,f] Mohit H. Adhikari,[c,f] Alan Miranda,[d,f] Liesbeth Vanherp,[f] Elisabeth Jonckers,[c,f] Philippe Joye,[d,f] Johan Van Audekerke,[c,f] Ignace Van Spilbeeck,[c,f] Marleen Verhoye,[c,f] Steven Staelens,[d,f] Daniele Bertoglio,[c,d,f] and Sarah Weckhuysen[a,b,e,f,*]

[a]Applied & Translational Neurogenomics Group, VIB Center for Molecular Neurology, VIB, Antwerp, 2610, Belgium
[b]Dept. of Neurology, University Hospital, Antwerp, 2610, Belgium
[c]University of Antwerp, Bio-Imaging Lab, Antwerp, 2610, Belgium
[d]University of Antwerp, Molecular Imaging Center Antwerp (MICA), Antwerp, 2610, Belgium
[e]Translational Neurosciences, Faculty of Medicine and Health Science, University of Antwerp, Antwerp, 2610, Belgium
[f]University of Antwerp, μNEURO Research Centre of Excellence, Antwerp, 2610, Belgium

eBioMedicine
2025;115: 105720
Published Online xxx
https://doi.org/10.1016/j.ebiom.2025.105720

Summary

Background Investigating dynamic changes during normal brain development is essential for understanding neurodevelopmental disorders (NDDs) and assessing the impact of novel therapies for these conditions. Rodent models, with their shorter developmental timeline, offer a valuable alternative to humans. This study aimed to characterise brain maturation in mice using a longitudinal, multimodal imaging approach.

Methods We conducted an *in vivo* imaging study on 31129/Sv mice with a complete longitudinal dataset available for 22 mice. Resting-state functional MRI (rs-fMRI), diffusion tensor imaging (DTI), and [^{18}F]SynVesT-1 PET were used to examine the development of brain functional connectivity (FC), white matter integrity, and synaptic density at three developmental stages: infancy (P14-21), juvenile (P32-42), and adulthood (P87-106).

Findings From infancy to juvenile age, we observed a significant decrease in FC and synaptic density, alongside increases in fractional anisotropy (FA) and decreases in mean, axial, and radial diffusivity (RD). From juvenile to adult age, synaptic density and FC stabilised, while FA further increased, and RD continued to decrease. The default mode like network was identifiable in mice across all developmental stages.

Interpretation Our findings mirror established patterns of human brain development, with infant mice allowing us to capture critical brain developmental changes, underscoring the translational relevance of our findings. This study provides a robust framework for normal rodent neurodevelopment and establishes a foundation for future research on NDDs in mice and the impact of novel treatments on neurodevelopment.

Funding Supported by the University of Antwerp, Fonds Wetenschappelijk Onderzoek (FWO), the Queen Elisabeth Medical Foundation, the European Joint Programme on Rare Disease, and Fondation Lejeune.

Keywords: Neurodevelopment; Resting-state functional magnetic resonance imaging; SV2A; Positron emission tomography; Diffusion tensor imaging

Introduction

Neurodevelopment is a dynamic process involving neurogenesis, synaptogenesis, myelination, and synaptic pruning, which collectively shape neurological pathways and influence brain function.[1] In humans, this process begins around gestational day 26 and continues into adulthood, with a critical period of rapid myelination and synaptogenesis extending from approximately 34 weeks of gestation to 2 years of age.[1,2] During this vulnerable period, the brain is particularly susceptible to genetic and/or environmental influences that can disrupt normal development leading to neurodevelopmental disorders (NDDs).[2]

NDDs affect up to 15–20% of children worldwide and cause significant lifelong challenges in cognition,

*Corresponding author. VIB-UAntwerp Center for Molecular Neurology, Universiteitsplein 1, Antwerp, 2610, Belgium.
E-mail address: Sarah.Weckhuysen@uantwerpen.vib.be (S. Weckhuysen).

Research in context

Evidence before this study

Capturing the dynamic changes of brain maturation is crucial for studying underlying neural mechanisms and improving therapies in neurodevelopmental disorders (NDDs). Rodents have been shown to have comparable brain developmental stages with humans, and, due to phenotypic variability and lengthy developmental timelines in humans, they offer a promising alternative for research. While individual imaging techniques such as resting-state functional MRI (rs-fMRI), diffusion tensor imaging (DTI), and positron emission tomography (PET) have been used to study various aspects of brain development, no studies had combined these approaches to provide a holistic view of neurodevelopment. Additionally, most previous studies focused on specific developmental stages or used cross-sectional designs, and only a few included rodents at infant age, the critical period of neurodevelopment, limiting our understanding of the continuous trajectory of brain maturation.

Added value of this study

This study provides a longitudinal examination of brain development in mice using a multimodal imaging approach that integrates rs-fMRI, DTI, and [^{18}F]SynVesT-1 PET. By capturing critical developmental changes from infancy to adulthood, we have identified that the most significant alterations in functional connectivity, white matter integrity, and synaptic density occur from infant to juvenile age, after which neurodevelopmental changes are more subtle. In particular, this study reveals high functional connectivity and synaptic density in infancy, which subsequently decline as fractional anisotropy increases. Importantly, these findings are consistent with patterns observed in human brain development.

Implications of all the available evidence

The multimodal and longitudinal design of this study, starting from infancy, allowed for a comprehensive characterisation of the complex brain maturational process. This robust framework can be used as a reference for future research into abnormal brain development in various rodent models of NDDs and the evaluation of the impact of novel treatments on neurodevelopment, ultimately contributing to improved therapeutic strategies for NDDs. The parallel between our findings and known patterns of human brain development highlights the potential of mouse models for studying neurodevelopmental processes and disorders, offering a promising tool for translational research in the field of neurodevelopment.

behaviour, and social functioning, highlighting the critical need for a deeper understanding of the underlying brain abnormalities and improved therapies.[3–5] However, studying abnormal neurodevelopment and evaluating potential interventions on neurodevelopment in humans is challenging due to phenotypic variability and lengthy developmental timelines.

Rodent models offer a promising alternative, as their neurodevelopment occurs on a considerably compressed timeline, beginning around gestational day 10 and reaching adulthood by approximately postnatal day 90 (P90).[1,2] This rapid progression, along with evidence of comparable brain developmental stages across species, positions rodents as invaluable preclinical models for studying NDDs and the effects of novel therapies.[1,2] To facilitate the *in-vivo* and non-invasive study of neurodevelopment, advanced imaging tools could play a critical role.

Diffusion tensor imaging (DTI) is a microstructural imaging technique that provides insights into the brain microstructure by analysing the quantitative diffusion of water molecules. Cross-sectional case-control DTI studies in humans and rodents have identified developmental changes and alterations in microstructural integrity associated with NDDs, which underlie impaired brain function and cognitive deficits.[6–10] Additionally, functional and molecular imaging techniques, such as resting-state functional MRI (rs-fMRI) and positron emission tomography (PET), have emerged as powerful tools for the non-invasive, longitudinal study of (ab)normal neurodevelopment in small animals and humans.[11] Rs-fMRI captures spontaneous low-frequency fluctuations of blood oxygenation level dependent (BOLD) signals, allowing the assessment of functional connectivity (FC) between brain regions.[12,13] Changes in FC can provide unique insights into neurodevelopment and underlying (patho)physiology in both humans and rodent models of NDDs.[14–23] PET imaging of the synaptic vesicle glycoprotein 2A (SV2A), using dedicated radioligand such as [^{18}F]SynVesT-1[24] provides a proxy for synaptic density.[25] Synaptic density and plasticity are critical determinants of neural circuit function and, by extension, cognitive processes. For instance, one PET study demonstrated an increase in brain synaptic density in rhesus monkey foetuses during the third trimester of pregnancy.[26] Furthermore, emerging research in various neurodegenerative disorders suggests that measuring synaptic density using PET may serve as a promising biomarker of cognitive function.[27,28]

Despite the potential of these advanced imaging modalities, no studies to date have employed a comprehensive longitudinal approach starting during the first postnatal weeks to characterise the trajectory of normal brain development in small-animal models.[11] In this study, we aim to fill this gap by investigating the trajectory of normal neurodevelopment in wild-type mice at three key developmental stages: infancy (P14-20),

adolescence (P32-42), and adulthood (P87-106). By integrating the complementary imaging modalities of rs-fMRI, [^{18}F]SynVesT-1 PET, and DTI, we seek to gain deeper insights into the functional, molecular, and microstructural changes occurring from infancy to adulthood. This comprehensive approach will provide a valuable reference for understanding the normal neurodevelopmental trajectory in mice and serve as a foundation for future studies investigating abnormal brain development and the effects of novel therapies on neurodevelopment in various rodent models of NDDs.

Methods

Animals

Adult 129Sv mice were purchased from Janvier labs and were used for breeding. This strain was selected because our lab has a genetic mouse model based on it, enabling future comparisons, and because existing DTI data for this strain are currently unavailable. The resulting pups, born in our facility, were used for the study. Experiments were performed on a total of 16 male and 15 female 129Sv mice between P14 and P106. Mice were initially housed with their dam and were weaned at P21. Subsequently, animals were group-housed in cages with a maximum of 8 mice per cage in a temperature and humidity-controlled environment with a 12 h/12 h light/dark cycle and access to food and water ad libitum.

Experimental design

A total of 31 mice underwent two imaging sessions at three different developmental stages (P14-P21 (infant age), P32-42 (juvenile age), and P87-106 (adult age)), with a minimum interval of 48 h between each session (Fig. 1a). Due to poor data quality caused by excessive movement during rs-fMRI (3 at P14-15 and 1 at P36), sudden death after rs-fMRI (1 at P14 and 1 at P35), issues with the injection of the PET tracer (1 at P18), and unsuccessful tail vein catheterisation (2 at P18), scans from 9 animals (7 at infant age and 2 at juvenile age) were excluded. This resulted in a final longitudinal cohort of 22 mice, with an equal sex distribution of 11 males and females.

Acquisition and data processing

Rs-fMRI and DTI procedure

Animals were initially anaesthetised with isoflurane (Forene, Belgium) in a gas mixture of 70% N_2 and 30% O_2 (induction 5%, positioning in scanner bed 2.5%). Mice were positioned in the scanner in the prone position with the head secured in a face mask using ear and a tooth bars. An anaesthesia protocol optimised by Grandjean et al. (2014)[29] to preserve cortical and subcortical FC and similar to that in our previous rs-fMRI work[30–32] was used. Following a bolus injection of 0.05 mg/kg of medetomidine hydrochloride (s.c., Domitor, Pfizer, Germany, catalogue # 1070499) to sedate the animals, the isoflurane was reduced to 1% (Fig. 1b). Ten minutes after the bolus injection, a continuous infusion of medetomidine (s.c., 0.1 mg/kg/h) was started, and the isoflurane was gradually reduced to 0.5% over the following 25 min. Thirty minutes after the start of the medetomidine infusion, the 10-min rs-fMRI acquisition was started. After scanning, animals received an injection of 0.25 mg/kg of atipamezole (s.c., Antisedan, Pfizer, Germany, catalogue # 1300185) to reverse the effects of medetomidine. Throughout the imaging procedure, body temperature was measured and maintained at (37.0 ± 0.5) °C using a rectal thermistor with a feedback-controlled warm air circuit (MR-compatible Small Animal Heating System, SA Instruments, Inc., USA). Respiratory rate was monitored throughout the experiment using a pressure-sensitive sensor (MR-compatible Small Animal Monitoring and Gating System, SA Instruments, Inc., USA).

MRI data were acquired using a 7T Pharmascan MR system (Bruker, Germany) and ParaVision 6.0.1 software (Bruker, Germany). Images were acquired using a standard Bruker cross-coil setup with a quadrature volume radiofrequency (RF) transmit coil and a quadrature surface RF receive coil for the mouse brain.[33] The duration of each scanning session ranged from 50 min to 1 h and consisted of four parts. First, three orthogonal T_2-weighted Turbo Rapid Acquisition with Relaxation Enhancement (RARE) images were acquired to uniformly position the slices (Repetition Time (TR) 2500 ms, effective Echo Time (TE) 33 ms, 9 slices, 0.5 mm thickness). Second, field maps were acquired for each scan session to assess field homogeneity, followed by local shimming to correct for inhomogeneity within the brain. Third, coronal diffusion-weighted (DW) MRI images were acquired using a two-shot spin-echo echo planar imaging (SE-EPI) sequence. The sequence included 30 DW images with 30 optimally distributed diffusion gradient directions, along with 3 non-DW images. The imaging parameters were as follows: TR 7000 ms, TE 23 ms, diffusion gradient pulse duration δ 4 ms, diffusion gradient separation D 12 ms, and b-value 1000 s/mm^2. The acquisition was limited to 16 slices of 0.4 mm thickness, covering only the cerebrum, with a slice interval of 0.1 mm. These parameters resulted in a total scan duration of 7 min and 42 s. The field-of-view (FOV) was set to (21.6 × 20.3) mm^2, and the matrix size was [108 × 10], yielding pixel dimensions of (0.2 × 0.2) mm^2.

Finally, a 10-min axial rs-fMRI scan was acquired using a T_2*-weighted gradient-echo EPI sequence (TR 1000 ms, TE 19 ms, 12 slices of 0.5 mm, slice interval of 0.1 mm, 600 repetitions). The field-of-view (FOV) was (25.6 × 19.2) mm^2 and the matrix size was [96 × 112], yielding pixel dimensions of (0.267 × 0.171) mm^2. For a subset of mice (n = 10), a 35 min T_2-weighted 3D RARE scan of the whole brain was acquired with the following parameters: TR 1800 ms, TE 42.6 ms, and RARE factor

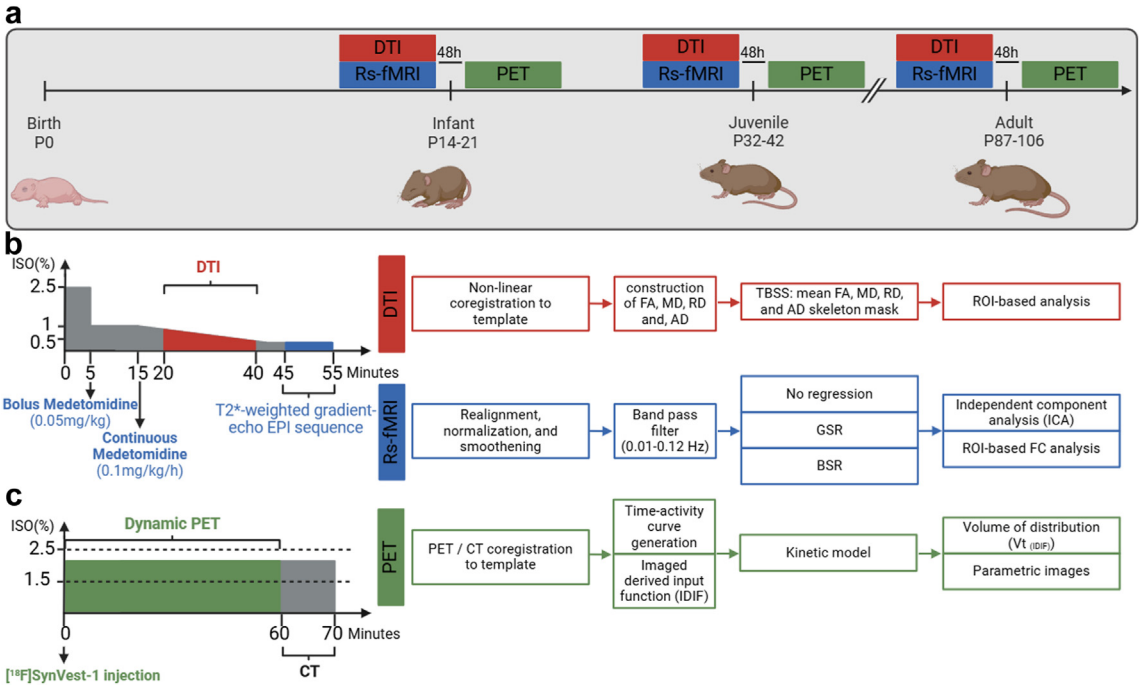

Fig. 1: **Experimental design, imaging, and analysis procedures for assessing brain development in mice at three key developmental stages.** (**a**) Resting-state functional MRI (rs-fMRI) and diffusion tensor imaging (DTI) were performed during the same session, followed by [^{18}F] SynVesT-1 positron emission tomography (PET) imaging at least 48 h later. (**b**) Imaging and analysis procedures for DTI and rs-fMRI. (**c**) Imaging and analysis procedures for PET and computed tomography (CT). AD: axial diffusivity, BSR: blood vessel signal regression, EPI: echo planar imaging, FA: fractional anisotropy, GSR: global signal regression, ISO: isoflurane, MD: mean diffusivity, RD: radial diffusivity, ROI: region-of-interest, TBSS: tract-based spatial statistics. Created with BioRender.com.

12. The FOV was (20 × 20 × 10) mm^3 and the acquisition matrix was [256 × 192 × 64], resulting in a spatial resolution of (0.078 × 0.104 × 0.156) mm^3. After scanning, the animals recovered under an infrared lamp and were transferred back to their home cage.

Rs-fMRI data processing and analysis

Rs-fMRI data pre-processing was performed using SPM12 software (Statistical Parametric Mapping, http://www.fil.ion.ucl.ac.uk) in MATLAB 2021a (MathWorks, USA) as previously described by our group.[31] All repetitions within a single scan were realigned to the first repetition using a least squares approach and a 6-parameter rigid body spatial transformation. The motion estimates were saved to be regressed from the data in a next step. A study specific EPI template per age was created in Advanced Normalisation Tools (ANTs) using the first repetition of each individual EPI dataset. We employed age-specific templates to ensure accurate and reliable analysis of mouse brain structures, because significant anatomical and volumetric changes occur between infant and juvenile ages.[34] The realigned rs-fMRI data were registered to their respective age-specific EPI template. Next, in plane smoothing was performed on the remaining dataset using a Gaussian kernel with full width at half maximum of twice the pixel size (0.534 × 0.342) mm^2. Finally, a bandpass filter (0.01–0.12 Hz) was applied using the Butterworth filter in MATLAB 2021a to preserve low frequency fluctuations in the BOLD signal time course. In one sub-analysis, global signal regression (GSR) was performed to correct for covariance between voxel-wise BOLD signals and the mean BOLD signal averaged over all voxels within a whole-brain mask. In a second sub-analysis, regression of the main blood vessel component signal (BSR) identified by independent component analysis (ICA) (see infra) was performed by delineating voxels of the superior sagittal sinus and extracting a region-of-interest (ROI) average value for each repetition in the time series.

Two different types of rs-fMRI data analysis were carried out. First, a data-driven approach, ICA, was performed to visualise clusters of voxels with similar BOLD fluctuation patterns over time.[35] We used the GIFT-Toolbox (Group ICA of fMRI toolbox: http://icatb.sourceforge.net/), which implements spatial ICA and estimates statistically independent sources.[33] Group ICA was performed on concatenated data from all animals per developmental stage using the Infomax algorithm. The number of components was set to 15, a value

suitable for identifying networks in mice.[36,37] Regional labelling of the different ICA components was performed using the Allen mouse anatomical brain atlas.[38]

Second, a region of interest (ROI)-based FC analysis[39] was performed to assess the FC between different regions. Using MRIcron software (version 1.0), ROIs were manually delineated on each age-specific EPI template, based on the anatomical regions present in the ICA maps and the Allen mouse brain atlas.[38] The following ROIs were considered: cingulate cortex (Cg), retrosplenial cortex (Rs), entorhinal cortex (Ent), hippocampus (HC), orbitofrontal cortex (Orb), temporal association cortex (TeA), parietal association cortex (PA), prelimbic cortex (PreL), visual cortex (VC), auditory cortex (AUD), olfactory cortex (Olf), somatosensory cortex (SS), motor cortex (Mot), caudate putamen (CPu), frontal association cortex (FrA), thalamus (Thal), and cerebellum (CB). All ROIs were delineated separately for the left and right hemispheres. Signal time courses were extracted for each ROI and correlation coefficients between signal time courses for each pair of ROIs were calculated and z-transformed (MATLAB 2021a). The average z-transformed correlation values were plotted in a FC matrix. In addition, FC strengths within a ROI were calculated by averaging the FC values between that given ROI and all other ROIs. Last, FC strengths within FC networks were determined by calculating the average of the pairwise correlation values between their components. The different networks were the default mode like network (DMLN) (Cg, Rs, Ent, HC, Orb, TeA, PA, and PreL), the associated cortical network (ACN) (VC, AUD, and Olf), and the lateral cortical network (LCN) (SS, Mot, CPu, and FrA).[40]

DTI data processing and analysis

DTI metrics, including fractional anisotropy (FA), mean diffusivity (MD), axial diffusivity (AD), and radial diffusivity (RD), were calculated in the native space of each animal using MRtrix3 (version 3.0.4).[41] Both the non-diffusion b0 image and the FA metric were utilised to create a multivariate study-specific template per age (ANTs). The warped FA images were then processed to generate a mean FA skeleton (white matter, WM) per age using the tract-based spatial statistics (TBSS) pipeline in FMRIB Software Library (FSL, version 5.0) (Figure S1).[42] A ROI encompassing the corpus callosum was manually drawn on each mean FA skeleton, with its anatomical location determined by referencing the Allen Mouse Brain Atlas. Next, grey matter (GM) ROIs, identical to the ROIs used for rs-fMRI analysis, were delineated on each age-specific template. The mean FA skeleton masks for each age group, including the corpus callosum ROI, and the GM ROIs were back-transformed to the individual space of each animal. Subsequently, individual mean values for FA, MD, AD, and RD were quantified for both the skeleton, the corpus callosum ROI, and the GM ROIs using MATLAB 2021a.

[^{18}F]SynVesT-1 PET imaging procedure

The synthesis of [^{18}F]SynVesT-1 was performed using a Trasis AllInOne synthesiser (Belgium) with a custom-built cassette as previously described.[24] At the end of synthesis, mean molar activity was 173.5 GBq/μmol ± 52.5 standard deviation (*SD*). Dynamic 60-min [^{18}F]SynVesT-1 microPET/Computed tomography (CT) images were acquired using two Siemens Inveon PET/CT scanners (Siemens Preclinical Solution, Knoxville, USA) (Fig. 1c). Animals were anaesthetised with isoflurane in medical oxygen (induction 5%, maintenance 1.5–2.5%). The animal's respiratory rate was monitored throughout the scanning procedure and the percentage of isoflurane was adjusted to maintain a respiratory rate between 80 and 100 breaths per minute. Body temperature was maintained at 37 ± 0.5 °C using a feedback-controlled warm air circuit (Minerve, France). Animals were administered an injection of 8.3 MBq ± 4.0 *SD* [^{18}F]SynVesT-1, corresponding to an injected mass of 5.8 nmol/kg ± 1.6 *SD*. The injection volume was 100 μL for infant mice and 200 μL for juvenile and adult mice, delivered at a rate of 1 ml/min using an automated pump (Pump 11 Elite, Harvard Apparatus, USA).

Immediately after the PET scan, a 10-min 80 kV/500 μA CT scan was performed for attenuation correction and anatomical reference. PET images were reconstructed with in-house developed list-mode ordered-subset expectation–maximisation (OSEM) reconstruction, considering a spatially variant resolution, with 16 subsets and 8 iterations, with attenuation correction performed using the attenuation map calculated from the CT scan.[43] Dynamic scans were reconstructed with framing of 12 frames × 10 s, 3 × 20 s, 3 × 30 s, 3 × 60 s, 3 × 150 s, and 9 × 300 s. PET image frames were reconstructed on a [128 × 128 × 159] grid of (0.776 × 0.776 × 0.796) mm^3 voxels.

[^{18}F]SynVesT-1 PET data processing and analysis

To create a 3D template for spatial normalisation of the [^{18}F]SynVesT-1 PET data, the 3D MRI images from each developmental stage (infant, juvenile, and adult) were combined to generate an age-specific template (ANTs). The 3D template was not used as the target space for rs-fMRI data processing, because co-registration of the infant EPI images with the 3D MRI template was not possible due to insufficient contrast between white and grey matter in 3D images at infant age. Bilateral ROIs were manually delineated on the 3D templates at each age in the PMOD 3.6 software using the Allen mouse brain atlas (Pmod Technologies, Zurich, Switzerland). The following ROIs were considered: whole brain, Olf, AUD, VC, primary SS (SS1), secondary SS (SS2), Mot, CPu, HC, Thal, pons, medulla, and CB, [^{18}F]SynVesT-1 PET data processing and analysis was performed using PMOD 3.6 software (Pmod Technologies, Zurich, Switzerland). Individual CT images were rigidly registered to the corresponding 3D MRI template using

automated spatial registration. The co-registration of PET and 3D MRI images was achieved by applying the same automated rigid registration approach, as the PET and CT were acquired on the same gantry. The output of the spatial registration was visually inspected for accuracy.

Regional time-activity curves (TACs) were extracted using ROIs. Kinetic modelling was performed using the Logan plot method with regional TACs and plasma activity (metabolite-corrected plasma/whole brain ratio-derived image-derived input function (IDIF)). The linear phase (t*) was determined from the curve fitting based on a maximum error of 10%, with t* ranging from 7.5 to 20 min. The total volume of the radioligand distribution ($V_{T\ (IDIF)}$) for each delineated ROI was measured by using an IDIF.[24] Average $V_{T\ (IDIF)}$ values for each ROI were obtained by grouping mice per age. Parametric whole brain images were generated using the pixel-wise modelling tool (PXMOD) of the PMOD 3.6 software. Group averages of the voxel-based graphical analysis of $V_{T\ (IDIF)}$ images (Logan plot) with plasma activity (metabolite-plasma/whole brain ratio-corrected IDIF) as the input function were generated and superimposed on the 3D MRI template for anatomical reference.

Statistics

Statistical analysis was performed using MATLAB 2021a (MathWorks, USA) for rs-fMRI data, and GraphPad Prism (v9.3) statistical software for DTI and [^{18}F]SynVesT-1 PET data. Prior to analysis, the assumption of normality for each imaging parameter was assessed using the Shapiro–Wilk test. The *P*-values for all imaging parameters were greater than 0.05, indicating that the normality assumption was met. Pairwise comparisons between age at the three developmental stages were conducted using a one-way repeated measures ANOVA. F-statistics and effect sizes (partial eta-squared, η^2_p) were reported to quantify the strength of effects. *P*-values were adjusted for multiple comparisons using the Benjamini and Hochberg false discovery rate (FDR) correction (All reported *P*-values reported throughout the manuscript are FDR corrected). The post-hoc power analysis was conducted using G*Power software (version 3.1.9.7) for a one-way repeated measures ANOVA with a within-subjects design. The analysis revealed that our sample size of 22 mice with complete longitudinal data achieved 100% power to detect the observed effects at a significance level of 0.05. The correlation among repeated measures was set at 0.5. Two-way repeated measures ANOVA was conducted to examine the interaction between age and sex on the imaging outcome parameters. Main effects and interactions were assessed, and *P*-values were adjusted for multiple comparisons using the Benjamini and Hochberg FDR correction.

To assess relationships between longitudinal changes in rs-fMRI, [^{18}F]SynVesT-1 PET, and DTI metrics (FA, MD, RD, AD), we calculated pairwise Pearson correlations between the changes in these parameters across nine overlapping ROIs using R (version 4.4.2). Changes were computed for two developmental periods: from infant to juvenile age, and from juvenile to adult age. For each ROI and time interval, we computed correlation matrices and corresponding *P*-values. Only correlations with $P < 0.05$ were considered significant.

Ethics

All animal experiments were performed in accordance with the European Committee Guidelines (Decree 2010/63/CEE) and in compliance with the 3 Rs (replacement, reduction, and refinement) principle and the ARRIVE guidelines. The study was approved by the Ethical Committee for Animal Testing at the University of Antwerp (Belgium) (permit number 2021-23). Animals were housed in the central animal facility of the University of Antwerp in accordance with the European guidelines (2007/526/EC).

Role of funders

The funders had no role in study design, data collection, data analyses, interpretation, or writing of report.

Results

Rs-fMRI

Twenty-two animals underwent DTI and rs-fMRI at infant (P14-17, median: P15), juvenile (P32-37, median: P34), and adult (P87-104, median: 94) ages. The body weight of the 22 animals ranged from 5.4 to 9.7 grams (g) at infant age (mean 7.7 g, *SD* 2.0), from 12.9 to 21.5 g at juvenile age (mean 16.6 g, *SD* 2.3), and from 18.2 to 29.0 g at adult age (mean 22.8 g, *SD* 2.8) (Figure S2a). The mean respiratory rate during the 10-min rs-fMRI scan was 134 (*SD* 33, range 90–210), 161 (*SD* 29, range 120–220), and 157 (*SD* 35, range 90–230) breaths per minute (bpm) at infant, juvenile and adult age, respectively (Figure S2b).

A group ICA analysis of 22 animals per group was performed as a data-driven approach to assess FC in the mouse brain at the three developmental ages. Components located in the brainstem or in the major blood vessels were excluded, resulting in ten components in the infant group, and eleven components in the juvenile and adult group (Table S1). Bilateral cerebellar, somatosensory, and CPu components, as well as the DMLN (Fig. 2) were identified at each age.

A ROI-based FC analysis was performed to investigate the FC of different brain networks (DMLN, ACN, and LCN) and their constituents. One-way repeated measures ANOVA revealed a significant age effect ($P = 0.003$, $F(2, 42) = 6.67$, $\eta^2_p = 0.25$), with reduced mean FC between infant and juvenile age in 317/561 (57%) connections both within and between different networks (Fig. 3a, Figures S3 and S4). There were no

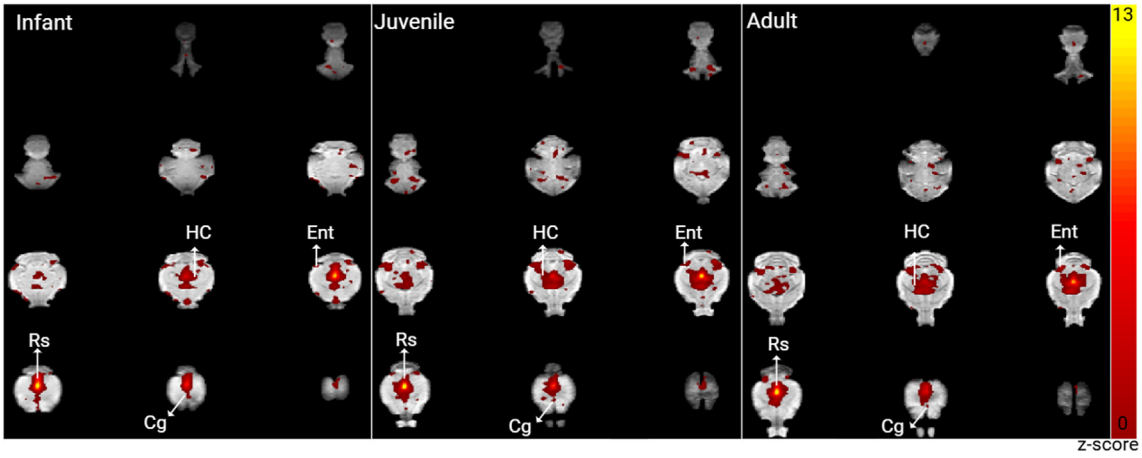

***Fig. 2:* Functional connectivity pattern showing the presence of the default mode like network (DMLN) using independent component analysis (ICA) of rs-fMRI data in mice at three different developmental stages.** Group level ICA demonstrates functional connectivity between key-constituents of DMLN: cingulate cortex (Cg), entorhinal cortex (Ent), hippocampus (HC), and retrosplenial cortex (Rs). The spatial colour-coded z-map of the ICA component (higher z-score represent stronger functional connectivity) is overlaid on the age-specific study-based EPI template.

significant FC differences between juvenile and adult age (Fig. 3b). Mean FC differed significantly in 49/561 (9%) connections between infant and adult age (Fig. 3c). In particular, FC decreased significantly from infant to adult age between regions of the LCN (mainly somatosensory cortex) and regions of the DMLN (27/49, 55%), and between the thalamus and the other networks (12/49, 24%).

The analysis of resting-state FC at the network level revealed significant developmental changes across different age groups (Figures S3 and S4). Specifically, we observed a significant decrease in FC from the infant to juvenile age between and within the DMLN, ACN, and LCN (median *P*-value = 0.004 (IQR: 0.003–0.006) [one-way repeated measures ANOVA, FDR corrected], median F-statistic = 6.053 (IQR: 5.990–7.345), median

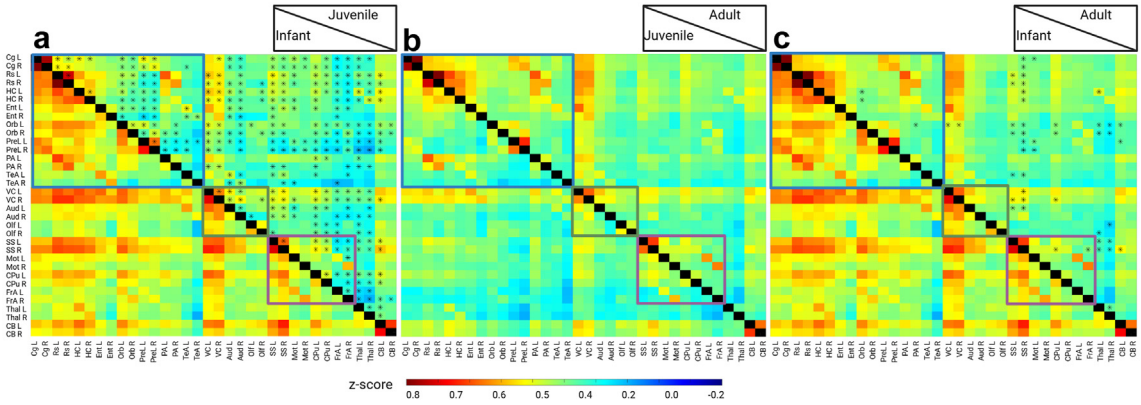

***Fig. 3:* Average functional connectivity (FC) matrices comparing FC data from two different neurodevelopmental stages (below vs above the diagonal). (a) Infant and juvenile, (b) juvenile and adult, and (c) infant and adult mice.** Each square represents the z-score of the Pearson correlation between a pair of regions of interest (ROIs), with the colour scale ranging from dark blue (negative correlation) to red (positive correlation). High z-scores represent a high correlation between the BOLD signal fluctuations of two ROIs, indicating a high FC between these regions. The large blue, green, and purple squares indicate the connections between regions within the default mode like network, associated cortical network, and lateral cortical network, respectively. Statistical analysis using one-way repeated measures ANOVA for age effects with Benjamini and Hochberg false discovery rate correction showed significantly higher FC between different ROIs in infant compared to juvenile and adult ages (*: $P < 0.05$). Cg: cingulate cortex, Rs: retrosplenial cortex, HC: hippocampus, Ent: entorhinal cortex, Orb: orbitofrontal cortex, PreL: prelimbic cortex, PA: parietal association cortex, TeA: temporal association cortex, VC: visual cortex, Aud: auditory cortex, Olf: olfactory cortex, SS: somatosensory cortex, Mot: motor cortex, CPu: caudate putamen, FrA: frontal association cortex, Thal: thalamus, CB: cerebellum, L: left, R: right.

η^2_p = 0.224 (IQR: 0.222–0.259)). In contrast, there were no significant differences in FC between the juvenile and adult ages indicating that FC levels stabilise during this period. Although the change in FC from juvenile to adult was not statistically significant, there was a slight increase in FC during this transition, particularly within the three networks (DMLN, ACN, and LCN), and between DMLN and ACN. Furthermore, although not statistically significant, reductions in FC between the DMLN and LCN (P = 0.07) as well as between the ACN and LCN (P = 0.07) were observed between infant and adult ages [one-way repeated measures ANOVA, FDR corrected].

To assess the effect of different physiological and non-physiological nuisances, GSR was applied on the rs-fMRI timeseries, followed by a ROI-based FC analysis (Figures S3–S5). Although no significant main effect of age was found (F(2, 42) = 2.132, P = 0.132, [one-way repeated measures ANOVA]), the partial eta squared value was moderate (η^2p = 0.096), suggesting that developmental changes may have a modest influence on FC across age groups. Nonetheless, post-hoc analyses revealed specific connections showing significant FC differences between certain age comparisons. For example, between infant and adult ages, 17 connections between regions of the DMLN and the LCN were significantly reduced. This pattern of FC changes was further corroborated by ROI-based analyses at the network level, indicating a consistent decrease in FC between the DMLN and LCN from infant to juvenile (P-value = 0.018), and infant to adult age (P-value = <0.001, [one-way repeated measures ANOVA, FDR corrected]), with the emergence of an anti-correlation between the two networks (Figures S3 and S4).

After the ICA-analysis, which showed a blood vessel component present at all developmental stages, BSR was performed to evaluate its impact on the ROI-based FC analysis (Figures S3, S4, and S6). Following the application of BSR, the ROI-based analysis revealed no significant main effect of age (F(2, 42) = 0.741, P = 0.627, η^2p = 0.023, [one-way repeated measures ANOVA]). Nonetheless, post-hoc analyses revealed specific connections showing significant decrease in FC from the infant to juvenile ages among several regions within the DMLN, and between the networks, including the thalamus. At the network level, a significant reduction in FC was noted between the DMLN and the LCN from the infant to juvenile age (P-value = 0.037, [one-way repeated measures ANOVA, FDR corrected], Figures S3 and S4).

To investigate whether the effects of age on FC between selected ROIs differ by sex, we conducted a two-way repeated measures ANOVA for males and females over time. This analysis revealed no significant interaction effect between sex and age (F(2, 42) = 1.89, P = 0.164, η^2p = 0.086, Figure S7).

DTI

Analysis of DTI data extracted from the WM skeleton and GM ROIs revealed widespread changes from infancy to adulthood. Across the three developmental stages, we observed a significant increase in WM FA values (F(2, 42) = 18.966, P = <0.0001, η^2p = 0.661) accompanied by a significant decrease in RD (F(2, 42) = 31.379, P = <0.0001, η^2p = 0.815, [one-way repeated measures ANOVA, FDR corrected], Fig. 4, Table S2). WM FA increased with 6.1% from infant to juvenile age and with 9.2% from juvenile to adult age, while RD decreased by 12.2% from infant to juvenile age followed by a further 3.4% decrease towards adult age. MD and AD decreased significantly (MD: F(2, 42) = 26.697, P = <0.0001, η^2p = 0.805; AD: F(2, 42) = 15.100, P = <0.0001, η^2p = 0.744, [one-way repeated measures ANOVA, FDR corrected]), with 11.0% and 9.4%, respectively, from infant to juvenile age. ROI analysis of the corpus callosum supported these findings (FA: F(2, 42) = 3.957, P = 0.0253, η^2p = 0.400; MD: F(2, 42) = 22.253, P = <0.0001, η^2p = 0.785; AD: F(2, 42) = 14.228, P = <0.0001, η^2p = 0.760; RD: F(2, 42) = 19.196, P = <0.0001, η^2p = 0.778, [one-way repeated measures ANOVA, FDR corrected]). It showed a 6.0% increase in FA between infant and juvenile age, accompanied by a 12.7%, 11.0%, and 14.0% decrease in MD, AD, and RD, respectively (Figure S8). In addition, significant differences in corpus callosum diffusion metrics between juvenile and adult mice included a 3.18% decrease in MD, and a 3.06% decrease in RD.

Next, DTI metrics in GM ROIs showed a significant age effect in all brain regions, except for FA in PreL L/R, Aud R, Olf L/R, and Mot L/R ((median values) FA: F(2, 42) = 17.710, P = <0.0001, η^2p = 0.482; MD: F(2, 42) = 95.658, P = <0.0001, η^2p = 0.834; AD: F(2, 42) = 72.378, P = <0.0001, η^2p = 0.792; RD: F(2, 42) = 118.692, P = <0.0001, η^2p = 0.862, [one-way repeated measures ANOVA], Figure S9). Post-hoc comparisons showed a significant increase in FA from infant to juvenile age, except in Cg L, PreL L/R, TeA L/R, Aud L/R, Olf L/R, SS L/R, Mot L/R, FrA R, and CB L, while MD, AD, and RD decreased significantly in all brain regions. From juvenile to adult age, FA further increased significantly in Cg L/R, Rs R, HC L, Ent L, PA L/R, TeA L/R, CPu R, Thal L/R, and CB L/R, while it decreased significantly in Orb R, Aud L, SS L/R, and FrA R. During the same time interval, MD, RD, and AD changed significantly in only a minority of ROIs with a significant decrease of MD in Olf L/R, of RD in PA L/R, TeA L, Olf L/R and CPu R, and of AD in Orb L/R and Olf L/R. In contrast, MD, RD, and AD increased significantly in CB.

To investigate whether the effects of age on diffusion metrics differ by sex, we performed a two-way repeated measures ANOVA of the WM diffusion metrics for males and females over time. This revealed no significant interaction effect between sex and age effect

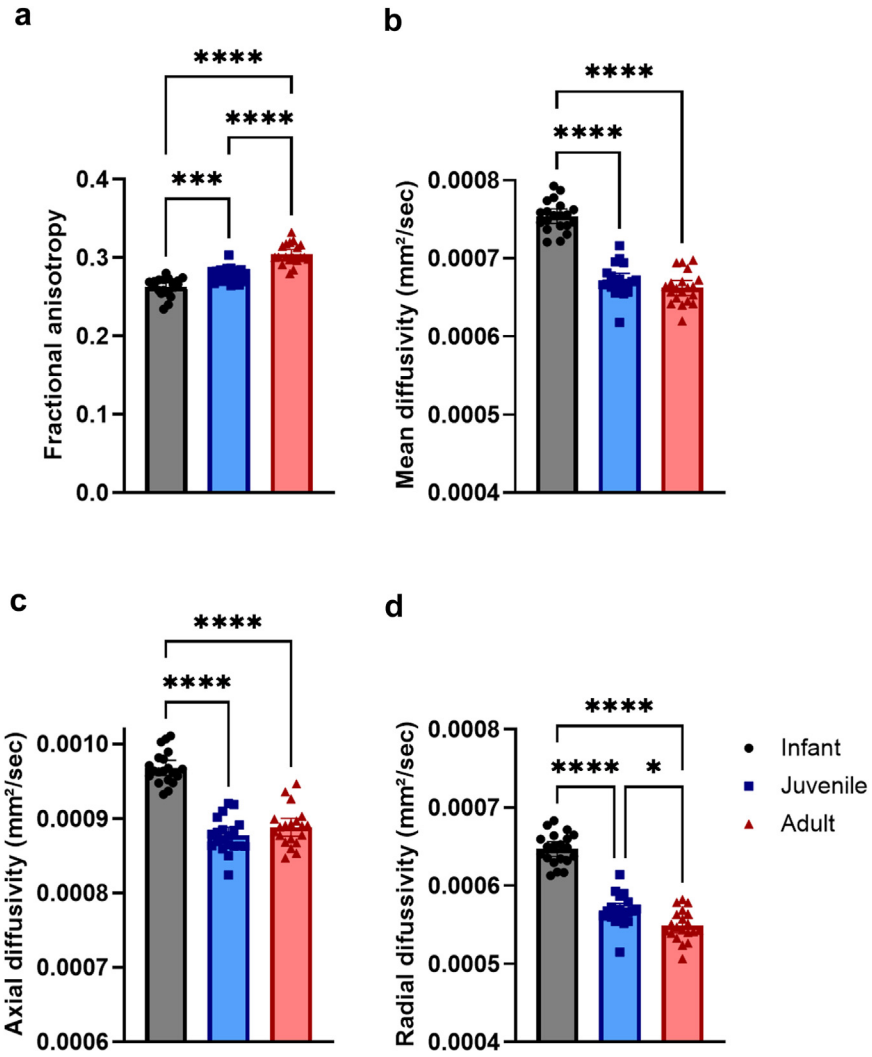

Fig. 4: **Developmental changes in white matter diffusion metrics across neurodevelopmental stages.** The figure presents the mean and individual values of fractional anisotropy (FA) (a), mean diffusivity (MD) (b), axial diffusivity (AD) (c), and radial diffusivity (RD) (d) at three developmental stages: infant (black), juvenile (blue), and adult (red). Statistical analysis using one-way repeated measures ANOVA with Benjamini and Hochberg false discovery rate correction for multiple comparisons showed significantly lower FA and higher MD, AD, and RD values at infant compared to juvenile age. FA increased and RD decreased significantly from juvenile to adult age (*: $P < 0.05$, ***: $P < 0.001$, ****: $P < 0.0001$).

($P = 0.098$–0.275, Figure S10). Despite the lack of a significant interaction, post-hoc comparisons indicated that females at infant age exhibited significantly higher FA (0.268 vs 0.2577, $P = 0.04$), as well as significantly lower MD (0.0007451 mm^2/s vs 0.0007628 mm^2/s, $P = 0.04$) and RD (0.0006368 mm^2/s vs 0.0006571 mm^2/s, $P = 0.02$) compared to males. Additionally, at the juvenile age, females showed significantly lower AD compared to males (0.0008659 mm^2/s vs 0.0008881 mm^2/s, $P = 0.04$).

[^{18}F]SynVesT-1 PET imaging

Twenty-two animals underwent [^{18}F]SynVesT-1 PET imaging to visualise SV2A density at infant (P16-21, median: P18), juvenile (P34-42, median: P36), and adult (P89-106, median: P96) ages. The body weight of the 22 animals ranged from 6.1 to 12.3 g at infant age (mean 8.6 g, *SD* 1.6), from 14.3 to 22.3 g at juvenile age (mean 17.8 g, *SD* 2.2), and from 16.9 to 35.0 g at adult age (mean 24.3 g, *SD* 3.9).

One-way repeated measures ANOVA revealed a significant age effect in all investigated brain regions (median P = <0.0001 (IQR: <0.0001–0.004), median $F(2,42) = 9.652$ (IQR: 5.965–17.711), median $\eta^2_p = 0.602$ (IQR: 0.522–0.684)). Regional [^{18}F]SynVesT-1 $V_{T\ (IDIF)}$ was significantly higher in infant mice compared to juvenile and adult mice in all investigated brain regions.

In adult mice, $V_{T\ (IDIF)}$ was significantly higher in cerebellum compared to juvenile mice, while no significant differences were observed in the other brain regions (Fig. 5, Table S3).

To investigate whether the effects of age on regional [^{18}F]SynVesT-1 $V_{T\ (IDIF)}$ differ by sex, we performed a two-way repeated measures ANOVA of the $V_{T\ (IDIF)}$ values for males and females over time. This analysis showed a significant sex*age interaction across all investigated brain regions (median P = 0.002 (IQR: 0.0018–0.0028), median F(2, 42) = 5.39 (IQR: 4.76–5.54), median η^2_p = 0.160 (IQR: 0.150–0.164)), indicating that the changes in the $V_{T\ (IDIF)}$ values across the developmental stages differ between males and females (Table S3, Figure S11). Post-hoc comparisons showed that the sex*age interaction was driven by the significant higher $V_{T\ (IDIF)}$ values found in females compared to males at juvenile age.

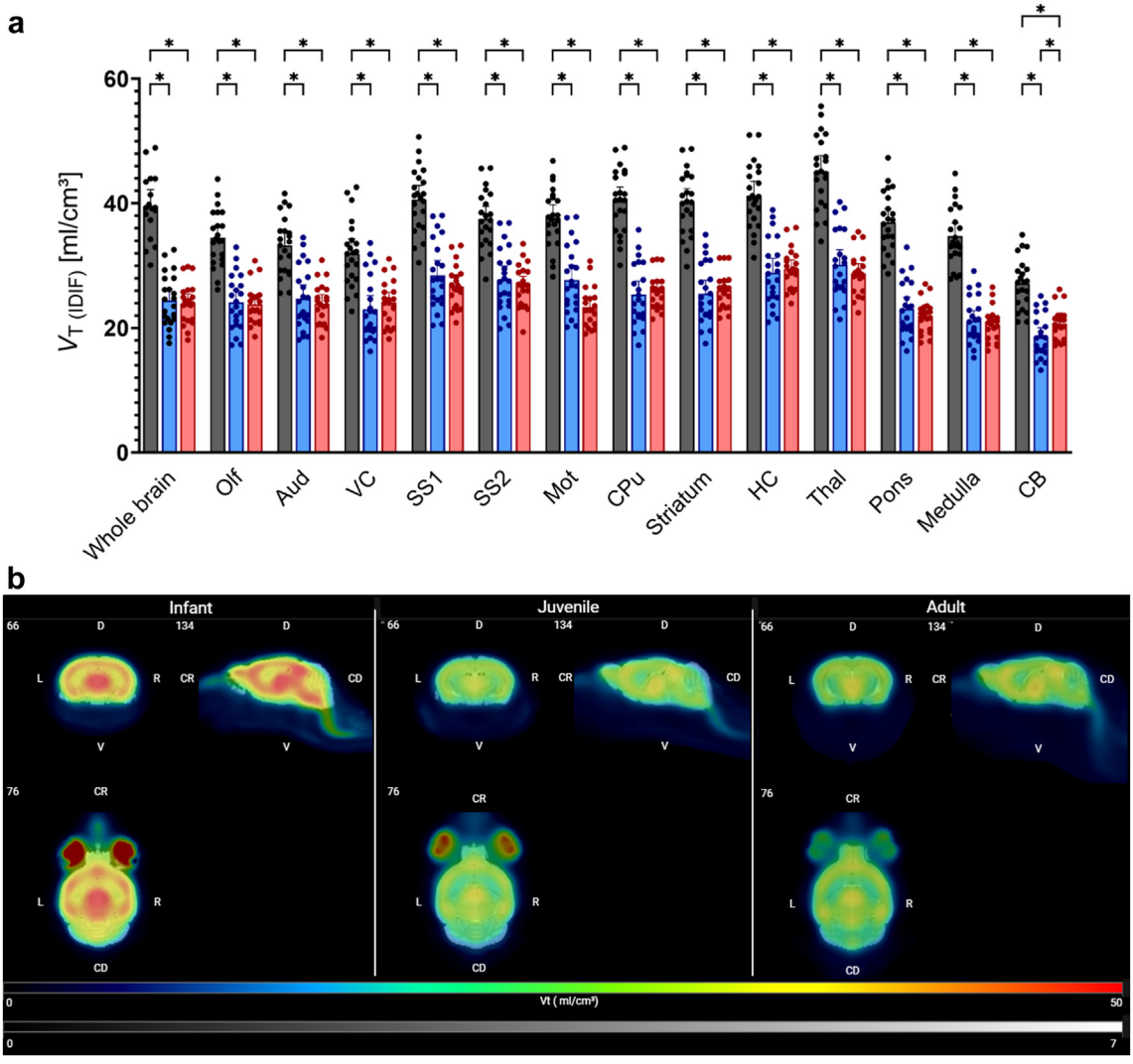

***Fig. 5:* Regional [^{18}F]SynVesT-1 volume of distribution ($V_{T\ (IDIF)}$) per developmental stage in different brain regions.** (a) [^{18}F]SynVesT-1 $V_{T\ (IDIF)}$ calculated with Logan plot. Black, blue, and red bars represent infant, juvenile, and adult age, respectively. The bar graphs present the mean $V_{T\ (IDIF)}$ with ±95% confidence interval. Statistical analysis using one-way repeated measures ANOVA with Benjamini and Hochberg false discovery rate correction showed significantly higher [^{18}F]SynVesT-1 uptake values at infant compared to juvenile and adult age in all brain regions (*: P < 0.05). (b) Mean parametric [^{18}F]SynVesT-1 images of each developmental stage displayed in coronal (top left), sagittal (top right), and axial (bottom left) views. Mean Vt values were higher in infant mice than in juvenile and adult mice (n = 22). Vt values (in ml/cm^3) are represented by a colour scale ranging from blue (0 ml/cm^3) to red (50 ml/cm^3). Olf: olfactory cortex, Aud: auditory cortex, VC: visual cortex, SS1: primary somatosensory cortex, SS2: secondary somatosensory cortex, Mot: motor cortex, CPu: caudate putamen, HC: hippocampus, Thal: thalamus, CB: cerebellum, CD: caudal, CR: cranial, D: dorsal, L: left, R: right, V: ventral.

Correlations between the imaging modalities

From infant to juvenile age, almost all imaging metrics (FC, Vt, MD, RD, and AD) decrease across all brain regions, except for FA which shows an increase (Figure S12). However, only MD, AD, and RD were significantly correlated across most regions (median r = 0.971 (IQR: 0.919–0.985), $P < 0.001$, [pairwise Pearson correlation], Figure S13). From juvenile to adult age, imaging metric changes are variable across brain regions (Figure S12). Apart for the correlated MD, AD, and RD metrices in most brain regions (median r = 0.952 (IQR: 0.910–0.978), $P < 0.001$, [pairwise Pearson correlation]), FA and FC-values were significantly anti-correlated with MD, AD and/or RD in only a minority of ROIs. Regional [^{18}F]SynVesT-1 $V_{T\ (IDIF)}$ was not significantly correlated with rs-fMRI or DTI metrics.

Discussion

In this study, we investigated *in-vivo* functional, molecular, and microstructural neurodevelopmental changes from infancy to adulthood in mice using longitudinal rs-fMRI, DTI, and [^{18}F]SynVesT-1 PET imaging of the same mice at infant (P14-21), juvenile (P32-42), and adult (P87-106) ages. We showed that resting-state FC and synaptic density generally decrease from infant to juvenile age, while WM and GM FA increase during this stage of brain development. From juvenile to adult age, we observed significant higher FA and lower RD in WM and in some GM regions (FA: Cg L/R, Rs R, HC L, Ent L, PA L/R, TeA L/R, CPu R, Thal L/R, and CB L/R; RD: PA L/R, TeA L, Olf L/R, and CPu R). Other imaging parameters remained mainly unchanged, such as resting-state FC, synaptic density, and AD and MD (WM and GM). Understanding the physiological basis of these changes is essential for elucidating the normal maturation processes of the brain and the potential impacts of various NDDs.

We employed rs-fMRI to investigate the maturation of brain FC in mice. First of all, at infant age, corresponding to approximately 1.5–2 years of age in humans, we already observed the presence of a DMLN (with the strongest FC between the core regions Cg, Rs, HC, and Ent) and a highly synchronised brain exhibiting high FC both between and within networks. These findings align with cross-sectional human rs-fMRI studies showing that primary as well as some higher-order networks, such as the default mode network (DMN), are synchronised by 1 year of age.[44] While some studies- and species-specific differences exist in the topography of the DMN, it has been consistently identified in humans, non-human primates, and rodents, underscoring its evolutionary conservation and its fundamental role in neurodevelopment.[45,46]

Secondly, from infancy to juvenile age, we observed an overall decrease in FC. To the best of our knowledge, only one rodent study has investigated normal neurodevelopment using rs-fMRI from infancy to juvenile age. This cross-sectional study used deep anaesthesia (2% isoflurane) in Wistar rats and reported increased FC between the hippocampus and orbitofrontal cortex from P21 to P39 using seed-based analysis.[47] These higher dosages of isoflurane have been shown to result in more widespread FC correlations, which may account for the differences observed in our study. Additionally, there is a lack of longitudinal human rs-fMRI studies focussing on comparable age intervals to those in our study.

We identified a few exceptions to the overall decrease in FC. Specifically, FC between the olfactory cortices and the DMLN regions, and the somatosensory and motor cortices, as well as between the motor cortices and other regions of the LCN, remained stable throughout development. We propose that this stability reflects the early maturation of these networks, which may be linked to survival needs.

Finally, from juvenile to adult age, we observed a non-significant trend of increased FC, primarily within the networks. This aligns with the subtle changes observed in one rat and several human rs-fMRI studies across these ages.[48–53] This suggests that while some maturation of functional networks occurs during this developmental period, major shifts may no longer be evident.

After applying GSR or BSR, we observed fewer reductions in functional connections from infant to juvenile age, with only a significant decrease in FC between regions of the DMLN and LCN. This indicates that the BOLD signals are largely influenced by large blood vessels and global noise. However, the application of GSR or BSR remains controversial, as we cannot completely exclude the possibility of neuronal contributions to the signals. Studies by Thompson et al. have shown that the global fMRI signal correlates with neural activity fluctuations[54] and metabolic shifts across brain states,[55] suggesting that GSR may inadvertently remove meaningful neural and metabolic information critical for understanding brain network dynamics. Age-related differences in the haemodynamic response could further affect FC quantification.[56] In addition to the decrease in FC, following GSR, an anti-correlation emerged at juvenile age between regions of the DMLN and LCN, persisting into adulthood. This anti-correlation must be interpreted cautiously, as GSR can introduce artefactual anti-correlations.[57] Nevertheless, the complementary roles of these networks (task-negative vs task-positive) are well-established, and multiple studies have demonstrated the existence of an anti-correlation between these two networks and its importance in normal neurodevelopment.[58,59]

Next, we used longitudinal DTI to investigate microstructural WM and GM brain development by measuring various diffusion metrics, including FA, MD, AD, and RD. We found increasing FA and

decreasing MD, AD, and RD with age in WM and most GM regions (FA: Cg R, Rs L/R, HC L/R, Ent L/R, Orb L/R, PA L/R, VC L/R, CPu L/R, Fra L, Thal L/R, and CB R; MD, AD, and RD: all ROIs [from infant to juvenile age], FA: Cg L/R, Rs R, HC L, Ent L, PA L/R, TeA L/R, CPu R, Thal L/R, and CB L/R; MD: Olf L/R; AD: Orb L/R and Olf L/R; RD: PA L/R, TeA L, Olf L/R, and CPu R [from juvenile to adult age]). The increased FA implies improved microstructural organisation of white matter and cellular structures, and the decreased diffusivity along all directions indicates myelination, increased fibre and cell density, and/or axon coherence.[60] Additionally, reduction in AD may result from an axonal pruning process.[61] Our findings are in line with several *in vivo* cross-sectional and limited longitudinal DTI studies conducted in humans and rodents from birth to adulthood.[61–66] Chahboune et al. (2007) studied FA and apparent diffusion coefficient (ADC) in four groups of C57B/L6 mice aged P15, P17, P38, and P45 with DTI. They observed increasing FA in CC, CPu, and Cg, while FA did not change significantly in the SS. In addition, ADC decreased significantly in all regions, except for the CPu.[66] These results are similar to what has been observed in the current study, except that we also found significantly decreased MD in the CPu. The discrepancy in the CPu could be attributed to methodological differences in calculating ADC versus MD. While ADC is derived from the trace of the diffusion tensor, MD is the mean of the eigenvalues of the tensor and can be influenced by differences in acquisition parameters or post-processing methods. Additionally, subtle strain-specific differences between SV/129 and C57BL/6 mice may play a role.

Finally, we performed [^{18}F]SynVesT-1 PET to assess synaptic density changes across different neurodevelopmental stages by quantifying SV2A receptor binding. We demonstrated a reduction in SV2A receptor binding from infant to juvenile age, followed by stabilisation until adulthood. To our knowledge, only one study has investigated brain development using PET quantification of SV2A binding, and only at foetal age. In this study, pregnant rhesus monkeys were scanned twice during the third trimester, showing increasing synaptic density with the highest SV2A binding in primary motor and visual regions during this period.[67] *Ex-vivo* histological studies of human brain tissue have revealed that synaptic density rapidly increases from foetal age until the first years of life, reaching higher levels than in adults.[68–70] Around 2–3.5 years of age, synaptogenesis plateaus and synaptic pruning occurs. This synapse elimination mainly takes place during the first decade, until late childhood or adolescence, but may extent until early adulthood.[68–70] Various *in-vivo* and *ex-vivo* rodent studies, using 2-photon microscopy and electron microscopy, respectively, have shown that during adolescence and adulthood there is a continued process of synapse elimination and formation associated with learning and adaptation. The interplay of these processes could maintain a relatively constant synaptic density despite ongoing remodelling of neural circuits, similar to our findings.[71–73] Additionally, our findings align with a broader pattern of neurodevelopmental changes observed in humans through various *in-vivo* PET studies, which have shown that cerebral glucose metabolism, blood flow, $GABA_A$ receptor density, and serotonin synthesis peak during the first years of life, after which they decline to adult values.[11]

This study utilises [^{18}F]SynVesT-1 PET to investigate synaptic density changes from infancy to adulthood in mice. The blood-brain barrier (BBB) permeability of the PET tracer is an important consideration in interpreting these findings. Notably, the BBB in mice is largely functional by embryonic day 15.5.[74] Additionally, our prior characterisation of SV2A PET radioligands, including [^{11}C]UCB-J,[75] [^{18}F]SynVesT-1,[24] and [^{18}F]UCB-J[76] has not revealed any significant BBB permeability issues in adult mice. Importantly, our use of dynamic kinetic modelling with heart-derived input functions ensures reliable quantification of synaptic density, independent of potential alterations in BBB permeability. Last, the juvenile and adult V_T values observed are consistent with previous studies in adult mice,[24] supporting the robustness of our findings.

Next to developmental changes over age, we also investigated interactions between age and sex. Our results revealed no significant age-by-sex interaction effects in the rs-fMRI and DTI data, indicating that the overall patterns of FC and diffusion metrics were consistent across sexes during the three developmental stages. This aligns with previous research suggesting that while sex differences may exist, they do not consistently manifest across all functional and microstructural developmental data or ages.[60,77–79] However, post-hoc comparisons of the DTI parameters showed that females exhibited higher FA and lower RD and MD at infant age, as well as lower AD at juvenile age compared to males. These findings indicate that females may have enhanced WM integrity during early development, which could be indicative of more advanced myelination or structural organisation at this stage. Multiple human DTI studies indeed showed the faster WM maturation in females compared to males with higher FA, and lower MD, AD, and RD at childhood age.[80–82] However, some DTI studies could not confirm these findings.[83,84] In the absence of a significant age-by-sex interaction effect, it indicates that the observed sex differences do not translate into broader developmental trends across the ages studied. Additionally, we observed a significant age-by-sex effect in our [^{18}F]SynVesT-1 PET data, primarily driven by the higher synaptic density in females compared to males at juvenile age. Neuron-synthesised oestrogen has been shown to induce synaptogenesis,[85,86] and thus could explain

differences in synaptic density during puberty. Our findings highlight the importance of considering developmental stages and sex when interpreting neurodevelopment.

This longitudinal study employs three complementary imaging techniques to provide a comprehensive view of brain development. Each modality contributes unique insights into specific aspects of brain maturation: rs-fMRI elucidates network interactions, [^{18}F]SynVesT-1 quantifies synaptic density, and DTI assesses microstructural organisation of tissues. While these processes are inherently interrelated during development, our findings reveal that correlations between the modalities are limited, emphasising the independent nature of SV2A availability from functional and structural dynamics. These findings underscore the importance of a multimodal approach to studying brain development, as each technique contributes complementary information about functional, structural, and molecular changes. Together, they provide a nuanced and comprehensive framework for characterising the dynamic processes shaping the brain during critical periods of maturation.

This study describes major brain developmental changes from infancy to adulthood in a large cohort of 22 mice using rs-fMRI, DTI and [^{18}F]SynVesT-1 PET. However, several limitations should be noted. First, our focus on three developmental stages provided valuable insights, but the timing of the developmental processes may differ in different brain regions.[64,68,87] More frequent sampling, particularly between infant and juvenile stages, could offer finer-grained insights into system-dependent changes. However, longitudinal studies using repeated anaesthesia over short periods of time are challenging as medetomidine requires several days to be completely metabolised. The potential influence of repeated anaesthesia on brain development is also a concern.[88] Alternative methods such as awake imaging are not feasible in young mice because such approaches often involve extensive habituation protocols and surgical intervention if this procedure involves head fixation, impeding longitudinal imaging in the same mice. Second, while this study offers an exploratory examination of brain development in rodents, the direct translation of these findings to humans is complex. Therefore, the results should be viewed as a foundational reference, with further investigation needed to confirm their relevance in the context of studying NDDs in preclinical models. Third, we acknowledge that varying the number of components may influence network delineation. The number of components in the ICA-analysis was set to 15 to facilitate comparison across ages, and was based on prior studies demonstrating that this value is suitable for identifying functionally relevant networks in mice.[36,37] Fourth, we acknowledge the potential influence of strain differences, such as those between the 129/Sv and the more commonly studied C57BL/6 strains. However, it is worth noting that DTI metrics in the 129/Sv strain are comparable to those reported for C57BL/6. These similarities provide some confidence in the broader applicability of our findings. Nonetheless, future studies exploring the profile of these metrics across other strains, including C57BL/6, will be valuable in further understanding potential strain-specific effects on neurodevelopmental processes. Last, as previously described, comparing brain regions across developmental stages is challenging due to differences in brain shape and size.[11] We addressed this by creating age-specific MRI and DTI templates and delineating brain regions based on a combination of ICA results, the Allen brain atlas tailored to each developmental stage, and the white matter skeleton generated by TBSS. However, inherent limitations associated with comparing brain regions across different ages remain. In conclusion, our longitudinal study utilising a multimodal imaging approach, combining rs-fMRI, DTI, and [^{18}F]SynVesT-1 PET, provides valuable insights into mouse brain development from infancy to adulthood, as it captures the complex, multifaceted nature of brain maturation. Our findings of decreasing FC and synaptic density, coupled with increasing white matter integrity from infant to juvenile stages, followed by stabilisation and further refinement into adulthood, mirror known patterns of human brain development. Importantly, the inclusion of an early developmental stage (P14-21) allowed us to investigate a critical period of brain maturation, often overlooked in rodent studies.

The parallel between our findings and human neurodevelopmental trajectories underscore the utility of mouse models in studying both normal and abnormal brain development. Our multimodal approach lays the groundwork for exploring interplay between structural, functional, and synaptic changes during critical maturation periods, enhancing our understanding of the neural underpinnings of cognition and behaviour. The comprehensive perspective offered by our study can inform future preclinical studies into various NDDs, potentially guiding more targeted research strategies and therapeutic interventions.

Contributors

Conceptualisation: S.W., D.B., S.S., M.V., E.J., L.V.; Data curation: C.M., N.V.G., P.J., J.V.A.; Formal analysis: C.M., N.V.G., M.H.A., A.M., J.V.A., I.V.S., D.B.; Project administration: E.J., P.J.; Writing–original draft: C.M., N.V.G., L.V., S.W.; Writing–review & editing: All authors. All authors read and approved the final version of the manuscript.

Data sharing statement

The imaging datasets generated during this study are available upon reasonable request from the corresponding author.

Declaration of interests

S.W. received consultancy and speaker fees from UCB, Xenon Pharmaceuticals, Lundbeck, Knopp Biosciences, Encoded Therapeutics, Angelini Pharma, and Roche.

Acknowledgements

This study was performed in collaboration with the MICA/BIL CORE facility of the University of Antwerp.

The authors thank Caroline Berghmans, Annemie Van Eetveldt, and Eleni Van der Hallen of the Molecular Imaging Center Antwerp (MICA) for their valuable assistance.

The computational resources and services used in this work were provided by the HPC core facility CalcUA of the Universiteit Antwerpen, the VSC (Flemish Supercomputer Center), funded by the Hercules Foundation and the Flemish Government – department EWI.

C.M. received support from the University of Antwerp (BOF DOCPRO4, project ID 42329). S.W. received support from Research Foundation–Flanders (FWO) Grants 1861424N, G041821N, and G056122N; the Queen Elisabeth Medical Foundation; the European Joint Programme on Rare Disease JTC 2020 (TreatKCNQ); and Fondation Lejeune. L.V., M.V., S.S., and S.W.: µNEURO center of excellence consortium received funding from the University of Antwerp (BOF Centre of Excellence, Project ID 50208).

Appendix A. Supplementary data

Supplementary data related to this article can be found at https://doi.org/10.1016/j.ebiom.2025.105720.

References

1 Semple BD, Blomgren K, Gimlin K, Ferriero DM, Noble-Haeusslein LJ. Brain development in rodents and humans: identifying benchmarks of maturation and vulnerability to injury across species. *Prog Neurobiol*. 2013;106–107:1–16.
2 Rice D, Barone S Jr. Critical periods of vulnerability for the developing nervous system: evidence from humans and animal models. *Environ Health Perspect*. 2000;108(Suppl 3):511–533.
3 Bosch R, Pagerols M, Rivas C, et al. Neurodevelopmental disorders among Spanish school-age children: prevalence and sociodemographic correlates. *Psychol Med*. 2022;52(14):3062–3072.
4 Naik SA, Shehzad N, Kawoosa AA, Kachroo A, Wani MA. Prevalence and spectrum of neurodevelopmental disorders in children aged 0-18 years Kashmir India. *Neurol India*. 2023;71(6):1297.
5 Yang Y, Zhao S, Zhang M, et al. Prevalence of neurodevelopmental disorders among US children and adolescents in 2019 and 2020. *Front Psychol*. 2022;13:997648.
6 Solso S, Xu R, Proudfoot J, et al. Diffusion tensor imaging provides evidence of possible axonal overconnectivity in frontal lobes in autism spectrum disorder toddlers. *Biol Psychiatry*. 2016;79(8):676–684.
7 Helmy E, Elnakib A, ElNakieb Y, et al. Role of artificial intelligence for autism diagnosis using DTI and fMRI: a survey. *Biomedicines*. 2023;11(7):1858.
8 Hasan KM, Kamali A, Abid H, Kramer LA, Fletcher JM, Ewing-Cobbs L. Quantification of the spatiotemporal microstructural organization of the human brain association, projection and commissural pathways across the lifespan using diffusion tensor tractography. *Brain Struct Funct*. 2010;214(4):361–373.
9 Snook L, Paulson L-A, Roy D, Phillips L, Beaulieu C. Diffusion tensor imaging of neurodevelopment in children and young adults. *Neuroimage*. 2005;26(4):1164–1173.
10 Blockx I, De Groof G, Verhoye M, et al. Microstructural changes observed with DKI in a transgenic Huntington rat model: evidence for abnormal neurodevelopment. *Neuroimage*. 2012;59(2):957–967.
11 Millevert C, Vidas-Guscic N, Vanherp L, et al. Resting-state functional MRI and PET imaging as noninvasive tools to study (ab) normal neurodevelopment in humans and rodents. *J Neurosci*. 2023;43(49):8275–8293.
12 Jonckers E, Van der Linden A, Verhoye M. Functional magnetic resonance imaging in rodents: an unique tool to study in vivo pharmacologic neuromodulation. *Curr Opin Pharmacol*. 2013;13(5):813–820.
13 Jonckers E, Shah D, Hamaide J, Verhoye M, Van der Linden A. The power of using functional fMRI on small rodents to study brain pharmacology and disease. *Front Pharmacol*. 2015;6:231.
14 Della Rosa PA, Canini M, Marchetta E, et al. The effects of the functional interplay between the default mode and executive control resting state networks on cognitive outcome in preterm born infants at 6 months of age. *Brain Cogn*. 2021;147:105669.
15 Graham AM, Buss C, Rasmussen JM, et al. Implications of newborn amygdala connectivity for fear and cognitive development at 6-months-of-age. *Dev Cogn Neurosci*. 2016;18:12–25.
16 Alcauter S, Lin W, Smith JK, et al. Development of thalamocortical connectivity during infancy and its cognitive correlations. *J Neurosci*. 2014;34(27):9067–9075.
17 Emerson RW, Gao W, Lin W. Longitudinal study of the emerging functional connectivity asymmetry of primary language regions during infancy. *J Neurosci*. 2016;36(42):10883–10892.
18 Zerbi V, Pagani M, Markicevic M, et al. Brain mapping across 16 autism mouse models reveals a spectrum of functional connectivity subtypes. *Mol Psychiatry*. 2021;26(12):7610–7620.
19 Pagani M, Bertero A, Liska A, et al. Deletion of autism risk gene Shank3 disrupts prefrontal connectivity. *J Neurosci*. 2019;39(27):5299–5310.
20 Liska A, Bertero A, Gomolka R, et al. Homozygous loss of autism-risk gene CNTNAP2 results in reduced local and long-range prefrontal functional connectivity. *Cereb Cortex*. 2018;28(4):1141–1153.
21 Zoratto F, Palombelli GM, Ruocco LA, et al. Enhanced limbic/impaired cortical-loop connection onto the hippocampus of NHE rats: application of resting-state functional connectivity in a preclinical ADHD model. *Behav Brain Res*. 2017;333:171–178.
22 Huang SM, Wu YL, Peng SL, et al. Inter-strain differences in default mode network: a resting state fMRI study on spontaneously hypertensive rat and Wistar Kyoto rat. *Sci Rep*. 2016;6:21697.
23 Poirier GL, Huang W, Tam K, DiFranza JR, King JA. Awake whole-brain functional connectivity alterations in the adolescent spontaneously hypertensive rat feature visual streams and striatal networks. *Brain Struct Funct*. 2017;222(4):1673–1683.
24 Bertoglio D, Zajicek F, Lombaerde S, et al. Validation, kinetic modeling, and test-retest reproducibility of [(18)F]SynVesT-1 for PET imaging of synaptic vesicle glycoprotein 2A in mice. *J Cereb Blood Flow Metab*. 2022;42(10):271678x221101648.
25 Finnema SJ, Nabulsi NB, Eid T, et al. Imaging synaptic density in the living human brain. *Sci Transl Med*. 2016;8(348):348ra96.
26 Li S, Cai Z, Zhang W, et al. Synthesis and in vivo evaluation of [(18)F]UCB-J for PET imaging of synaptic vesicle glycoprotein 2A (SV2A). *Eur J Nucl Med Mol Imaging*. 2019;46(9):1952–1965.
27 Colom-Cadena M, Spires-Jones T, Zetterberg H, et al. The clinical promise of biomarkers of synapse damage or loss in Alzheimer's disease. *Alzheimers Res Ther*. 2020;12(1):21.
28 Visser M, O'Brien JT, Mak E. In vivo imaging of synaptic density in neurodegenerative disorders with positron emission tomography: a systematic review. *Ageing Res Rev*. 2024;94:102197.
29 Grandjean J, Schroeter A, Batata I, Rudin M. Optimization of anesthesia protocol for resting-state fMRI in mice based on differential effects of anesthetics on functional connectivity patterns. *Neuroimage*. 2014;102(Pt 2):838–847.
30 Adhikari MH, Belloy ME, Van der Linden A, Keliris GA, Verhoye M. Resting-state co-activation patterns as promising candidates for prediction of Alzheimer's disease in aged mice. *Front Neural Circuits*. 2020;14:612529.
31 Vasilkovska T, Adhikari MH, Van Audekerke J, et al. Resting-state fMRI reveals longitudinal alterations in brain network connectivity in the zQ175DN mouse model of Huntington's disease. *Neurobiol Dis*. 2023;181:106095.
32 Belloy ME, Naeyaert M, Abbas A, et al. Dynamic resting state fMRI analysis in mice reveals a set of Quasi-Periodic Patterns and illustrates their relationship with the global signal. *Neuroimage*. 2018;180(Pt B):463–484.
33 Jonckers E, Van Audekerke J, De Visscher G, Van der Linden A, Verhoye M. Functional connectivity fMRI of the rodent brain: comparison of functional connectivity networks in rat and mouse. *PLoS One*. 2011;6(4):e18876.
34 Chuang N, Mori S, Yamamoto A, et al. An MRI-based atlas and database of the developing mouse brain. *Neuroimage*. 2011;54(1):80–89.
35 van de Ven VG, Formisano E, Prvulovic D, Roeder CH, Linden DE. Functional connectivity as revealed by spatial independent component analysis of fMRI measurements during rest. *Hum Brain Mapp*. 2004;22(3):165–178.
36 Sforazzini F, Schwarz AJ, Galbusera A, Bifone A, Gozzi A. Distributed BOLD and CBV-weighted resting-state networks in the mouse brain. *Neuroimage*. 2014;87:403–415.
37 Shah D, Deleye S, Verhoye M, Staelens S, Van der Linden A. Resting-state functional MRI and [18F]-FDG PET demonstrate

differences in neuronal activity between commonly used mouse strains. *Neuroimage*. 2016;125:571–577.
38 Wang Q, Ding SL, Li Y, et al. The allen mouse brain common coordinate framework: a 3D reference atlas. *Cell*. 2020;181(4):936–953.e20.
39 Biswal B, Yetkin FZ, Haughton VM, Hyde JS. Functional connectivity in the motor cortex of resting human brain using echo-planar MRI. *Magn Reson Med*. 1995;34(4):537–541.
40 Liska A, Galbusera A, Schwarz AJ, Gozzi A. Functional connectivity hubs of the mouse brain. *Neuroimage*. 2015;115:281–291.
41 Tournier JD, Smith R, Raffelt D, et al. MRtrix3: a fast, flexible and open software framework for medical image processing and visualisation. *Neuroimage*. 2019;202:116137.
42 Smith SM, Jenkinson M, Johansen-Berg H, et al. Tract-based spatial statistics: voxelwise analysis of multi-subject diffusion data. *Neuroimage*. 2006;31(4):1487–1505.
43 Miranda A, Bertoglio D, Glorie D, Stroobants S, Staelens S, Verhaeghe J. Validation of a spatially variant resolution model for small animal brain PET studies. *Biomed Phys Eng Express*. 2020;6(4):045001.
44 Gao W, Zhu H, Giovanello KS, et al. Evidence on the emergence of the brain's default network from 2-week-old to 2-year-old healthy pediatric subjects. *Proc Natl Acad Sci U S A*. 2009;106(16):6790–6795.
45 Pagani M, Gutierrez-Barragan D, de Guzman AE, Xu T, Gozzi A. Mapping and comparing fMRI connectivity networks across species. *Commun Biol*. 2023;6(1):1238.
46 Gutierrez-Barragan D, Ramirez JSB, Panzeri S, Xu T, Gozzi A. Evolutionarily conserved fMRI network dynamics in the mouse, macaque, and human brain. *Nat Commun*. 2024;15(1):8518.
47 Zoratto F, Altabella L, Tistarelli N, Laviola G, Adriani W, Canese R. Inside the developing brain to understand teen behavior from rat models: metabolic, structural, and functional-connectivity alterations among limbic structures across three pre-adolescent stages. *Front Behav Neurosci*. 2018;12:208.
48 Fair DA, Dosenbach NU, Church JA, et al. Development of distinct control networks through segregation and integration. *Proc Natl Acad Sci U S A*. 2007;104(33):13507–13512.
49 Fair DA, Cohen AL, Dosenbach NU, et al. The maturing architecture of the brain's default network. *Proc Natl Acad Sci U S A*. 2008;105(10):4028–4032.
50 Fair DA, Cohen AL, Power JD, et al. Functional brain networks develop from a "local to distributed" organization. *PLoS Comput Biol*. 2009;5(5):e1000381.
51 Supekar K, Musen M, Menon V. Development of large-scale functional brain networks in children. *PLoS Biol*. 2009;7(7):e1000157.
52 Supekar K, Uddin LQ, Prater K, Amin H, Greicius MD, Menon V. Development of functional and structural connectivity within the default mode network in young children. *Neuroimage*. 2010;52(1):290–301.
53 Kelly AM, Di Martino A, Uddin LQ, et al. Development of anterior cingulate functional connectivity from late childhood to early adulthood. *Cereb Cortex*. 2009;19(3):640–657.
54 Thompson GJ, Merritt MD, Pan WJ, et al. Neural correlates of time-varying functional connectivity in the rat. *Neuroimage*. 2013;83:826–836.
55 Thompson GJ, Riedl V, Grimmer T, Drzezga A, Herman P, Hyder F. The whole-brain "global" signal from resting state fMRI as a potential biomarker of quantitative state changes in glucose metabolism. *Brain Connect*. 2016;6(6):435–447.
56 Colonnese MT, Phillips MA, Constantine-Paton M, Kaila K, Jasanoff A. Development of hemodynamic responses and functional connectivity in rat somatosensory cortex. *Nat Neurosci*. 2008;11(1):72–79.
57 Murphy K, Birn RM, Handwerker DA, Jones TB, Bandettini PA. The impact of global signal regression on resting state correlations: are anti-correlated networks introduced? *Neuroimage*. 2009;44(3):893–905.
58 Gao W, Gilmore JH, Shen D, Smith JK, Zhu H, Lin W. The synchronization within and interaction between the default and dorsal attention networks in early infancy. *Cereb Cortex*. 2013;23(3):594–603.
59 Fox MD, Snyder AZ, Vincent JL, Corbetta M, Van Essen DC, Raichle ME. The human brain is intrinsically organized into dynamic, anticorrelated functional networks. *Proc Natl Acad Sci U S A*. 2005;102(27):9673–9678.
60 Lebel C, Deoni S. The development of brain white matter microstructure. *Neuroimage*. 2018;182:207–218.
61 Bockhorst KH, Narayana PA, Liu R, et al. Early postnatal development of rat brain: in vivo diffusion tensor imaging. *J Neurosci Res*. 2008;86(7):1520–1528.
62 Gilmore JH, Lin W, Corouge I, et al. Early postnatal development of corpus callosum and corticospinal white matter assessed with quantitative tractography. *AJNR Am J Neuroradiol*. 2007;28(9):1789–1795.
63 Larvaron P, Boespflug-Tanguy O, Renou JP, Bonny JM. In vivo analysis of the post-natal development of normal mouse brain by DTI. *NMR Biomed*. 2007;20(4):413–421.
64 Gao W, Lin W, Chen Y, et al. Temporal and spatial development of axonal maturation and myelination of white matter in the developing brain. *AJNR Am J Neuroradiol*. 2009;30(2):290–296.
65 Lebel C, Beaulieu C. Longitudinal development of human brain wiring continues from childhood into adulthood. *J Neurosci*. 2011;31(30):10937–10947.
66 Chahboune H, Ment LR, Stewart WB, Ma X, Rothman DL, Hyder F. Neurodevelopment of C57B/L6 mouse brain assessed by in vivo diffusion tensor imaging. *NMR Biomed*. 2007;20(3):375–382.
67 Rossano S, Toyonaga T, Berg E, et al. Imaging the fetal nonhuman primate brain with SV2A positron emission tomography (PET). *Eur J Nucl Med Mol Imaging*. 2022;49(11):3679–3691.
68 Huttenlocher PR, Dabholkar AS. Regional differences in synaptogenesis in human cerebral cortex. *J Comp Neurol*. 1997;387(2):167–178.
69 Huttenlocher PR. Synaptic density in human frontal cortex - developmental changes and effects of aging. *Brain Res*. 1979;163(2):195–205.
70 Petanjek Z, Judaš M, Šimic G, et al. Extraordinary neoteny of synaptic spines in the human prefrontal cortex. *Proc Natl Acad Sci U S A*. 2011;108(32):13281–13286.
71 Kleim JA, Lussnig E, Schwarz ER, Comery TA, Greenough WT. Synaptogenesis and FOS expression in the motor cortex of the adult rat after motor skill learning. *J Neurosci*. 1996;16(14):4529–4535.
72 Yang G, Pan F, Gan WB. Stably maintained dendritic spines are associated with lifelong memories. *Nature*. 2009;462(7275):920–924.
73 Trachtenberg JT, Chen BE, Knott GW, et al. Long-term in vivo imaging of experience-dependent synaptic plasticity in adult cortex. *Nature*. 2002;420(6917):788–794.
74 O'Brown NM, Pfau SJ, Gu C. Bridging barriers: a comparative look at the blood-brain barrier across organisms. *Genes Dev*. 2018;32(7–8):466–478.
75 Bertoglio D, Verhaeghe J, Miranda A, et al. Validation and noninvasive kinetic modeling of [(11)C]UCB-J PET imaging in mice. *J Cereb Blood Flow Metab*. 2020;40(6):1351–1362.
76 Everix L, Elvas F, Miranda Menchaca A, et al. Preclinical validation and kinetic modelling of the SV2A PET ligand [(18)F]UCB-J in mice. *J Cereb Blood Flow Metab*. 2024;271678x241304923. https://doi.org/10.1177/0271678X241304923.
77 Kaczkurkin AN, Raznahan A, Satterthwaite TD. Sex differences in the developing brain: insights from multimodal neuroimaging. *Neuropsychopharmacology*. 2019;44(1):71–85.
78 López-Vicente M, Lamballais S, Louwen S, et al. White matter microstructure correlates of age, sex, handedness and motor ability in a population-based sample of 3031 school-age children. *Neuroimage*. 2021;227:117643.
79 Tarchi L, Damiani S, Vittori PT, et al. Progressive Voxel-Wise Homotopic Connectivity from childhood to adulthood: age-related functional asymmetry in resting-state functional magnetic resonance imaging. *Dev Psychobiol*. 2023;65(2):e22366.
80 Asato MR, Terwilliger R, Woo J, Luna B. White matter development in adolescence: a DTI study. *Cereb Cortex*. 2010;20(9):2122–2131.
81 Simmonds DJ, Hallquist MN, Asato M, Luna B. Developmental stages and sex differences of white matter and behavioral development through adolescence: a longitudinal diffusion tensor imaging (DTI) study. *Neuroimage*. 2014;92:356–368.
82 Seunarine KK, Clayden JD, Jentschke S, et al. Sexual dimorphism in white matter developmental trajectories using tract-based spatial statistics. *Brain Connect*. 2016;6(1):37–47.
83 Krogsrud SK, Fjell AM, Tamnes CK, et al. Changes in white matter microstructure in the developing brain-a longitudinal diffusion tensor imaging study of children from 4 to 11 years of age. *Neuroimage*. 2016;124:473–486.

84 Lebel C, Walker L, Leemans A, Phillips L, Beaulieu C. Microstructural maturation of the human brain from childhood to adulthood. *Neuroimage*. 2008;40(3):1044–1055.
85 Iqbal J, Huang GD, Xue YX, Yang M, Jia XJ. Role of estrogen in sex differences in memory, emotion and neuropsychiatric disorders. *Mol Biol Rep*. 2024;51(1):415.
86 MacLusky NJ, Luine VN, Hajszan T, Leranth C. The 17alpha and 17beta isomers of estradiol both induce rapid spine synapse formation in the CA1 hippocampal subfield of ovariectomized female rats. *Endocrinology*. 2005;146(1):287–293.
87 Gao W, Gilmore JH, Giovanello KS, et al. Temporal and spatial evolution of brain network topology during the first two years of life. *PLoS One*. 2011;6(9):e25278.
88 Zhao X, Shi D, Du Y, et al. Repeated neonatal exposure to sevoflurane induces age-dependent impairments in cognition and synaptic plasticity in mice. *Dev Neurosci*. 2022;44(3):153–161.